Microsatellites Formation Flying for In-Situ Space Debris Detection

C. Cappelletti, F. Guarducci, F. Paolillo, L. Ridolfi, F. Graziani, M. L. Battagliere, F. Piergentili, F. Santoni

Abstract

Since nineties, the GAUSS (Group of Astrodynamics of the ”Sapienza” University of Roma) has started UNISAT program with the aim to design, manufacture and launch University microsatellites, completely built and operated in orbit by students of the school of Aerospace engineering. In the framework of this program four satellites have been launched, two years apart one from the other, starting in 2000, and a fifth satellite is nowadays under construction.
In the same period, GAUSS has also been involved in optical space debris surveillance, participating to the IADC (Inter-Agency Space Debris Coordination Committee) observation joint campaign and, more recently, by manufacturing the first Italian observatory completely dedicated to space debris monitoring.
Combining these two experiences GAUSS students, researchers and professors are analysing the feasibility of a formation flight mission in order to detect space debris, taking advantage of an in situ observation above Earth's atmosphere.
The paper deals with this space debris detection mission focussing on LEO orbital regime. As a matter of fact, these orbits are very crowded. Small (from 1 to 10 centimetres) debris in these orbits are difficult to detect and track by ground based optical systems. A constellation of satellites boarding optics and sensors sensible to infrared or visible radiation could monitor the LEO space debris environment through in-situ measurements. Moreover, a constellation of satellites flying in small formations permits to achieve not only debris detection but also preliminary orbit determination, thus simplifying follow-up ground base observations.
The paper gives an overview of the proposed constellation of satellites flying in small formations, highlighting main constraints, achievements and flaws of a few possible solutions.
The proposed mission configuration is made up of three satellites in a trailing formation. One satellite, the central one, will be responsible of detection and fast orbit determination of LEO objects. The other two smaller satellites will be able to track the object in order to allow a larger number of pictures and a better orbit determination.
Numerical simulations of these control strategies have been carried out taking into account different sensor accuracies; the results of some study cases are reported.
Two orbit control strategies are analyzed in order to keep the satellites within the formation constraints: the use of periodic maneuvers with chemical propulsion or a continuous counterbalance of the main perturbation (i.e. the aerodynamic one) with the use of Pulsed Plasma Thrusters.
In the end, sensors and optics feasible for this mission are analysed and two different image processing methods have been studied in order to achieve automatic in-orbit debris detection.

1. Introduction

Since nineties, the GAUSS (Group of Astrodynamics of the ”Sapienza” University of Roma) has started UNISAT program with the aim to design, manufacture and launch University

microsatellites, completely built and operated in orbit by students of the school of Aerospace engineering. In the framework of this program four satellites have already been launched, two years apart one from the other, starting in 2000, and a fifth satellite is nowadays under construction.

In 2002 G.A.U.S.S. (Group of Astrodynamics of the University of Rome "La Sapienza") also started out the Italian space debris observation activity [1]. In particular it has been carried out the Inter-Agency Space Debris Coordination Committee (IADC) co-ordinated campaigns addressed to the Geostationary Earth Orbit (GEO) observation [2]. In 2003 GAUSS conducted a very successful test campaign to prove the effectiveness of two-telescope GEO objects observation and orbit determination [3]. Moreover, same additional observation campaign for low Earth orbit satellites (LEO) orbit determination has been carried out [4]. All of these observations were performed using the facilities of the Associazione Astronomica Frusinate which operates the Campo Catino and the Collepardo observatories using the facilities kindly made available by Associazione Astronomica Frusinate (Frosinone Astronomical Society) and (in the case of the two-telescope campaign) by Observatori Astronòmic de Mallorca (Mallorca Astronomical Observatory).

In 2006 GAUSS designed and built for Agenzia Spaziale Italiana (Italian Space Agency, ASI) the first Italian optical observatory for space debris observation [8]. At present, the observatory has been completed and participates in IADC co-ordinated campaigns.

In this context, the feasibility of a formation flight mission in order to detect LEO orbit space debris has been analysed, taking advantage of an observation above Earth's atmosphere. The results of this analysis are presented on this paper.

The proposed mission configuration is made up of three satellites in a trailing formation. One satellite, the central one, will be responsible of detection and fast orbit determination of LEO objects. The other two smaller satellites will be able to track accurately objects upon indication of the mother satellite in order to allow a larger number of pictures and a better orbit determination.

An analysis of the orbital perturbations acting over the formation has been performed taking into account the effect of aerodynamic drag and Earth's oblateness. This analysis determines the time between two subsequent manoeuvres.

The satellite's Attitude Control will be based on reaction wheels, Earth Sensor and star tracker; the two smaller satellites will also have a tracking mode; this tracking mode is controlled by the use of reaction wheels and Rate Integrating Gyros.

All the formation satellite are equipped with a large FOV (Field of view) optical system with the aim of detecting a large number of objects. The satellites are able to perform on-board image analysis, in particular the bigger one which is able of a faster and higher resolution processing.

A software for the automatic image processing and debris detection has been developed, tacking into account orbital observation condition and the available optical system.

2. Mission profile and objectives

Low Earth Orbits are particularly affected by space debris due to the large exploitation of these orbital regimes by commercial and scientific missions.

Moreover these orbits have been recently interested by break-up event as the Chinese ASAT test, carried out against the Chinese FENGYUN 1C polar-orbiting weather satellite on 2007 January 11, which provided an increase in number of space debris.

The distribution of space debris at these heights is sketched in figure 1, (Blue line reports situation before the ASAT test and red line after the test)

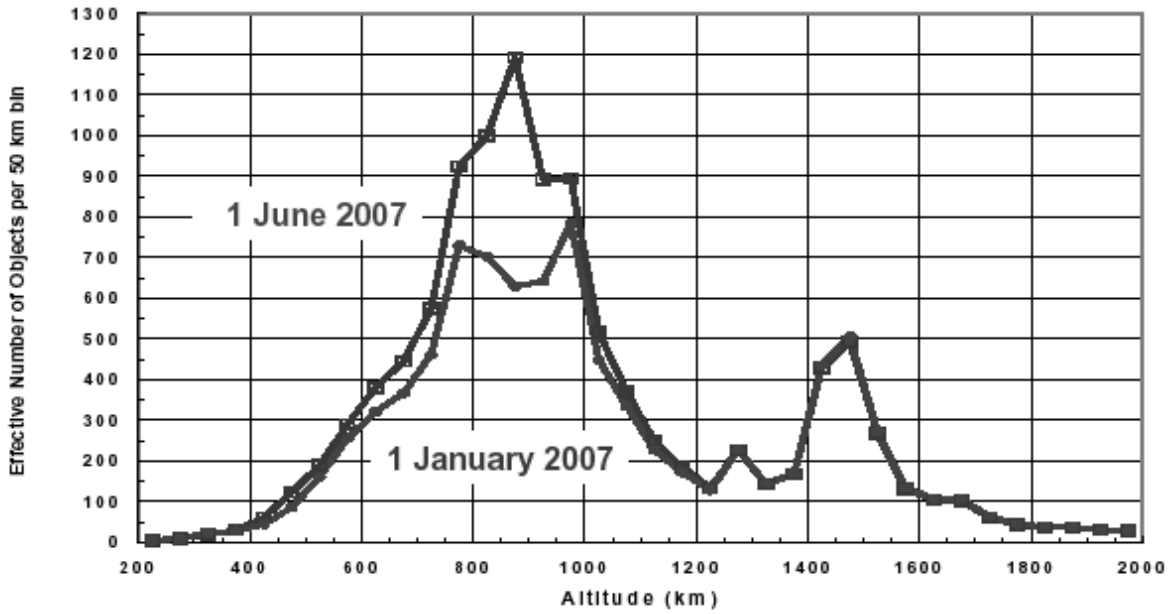

Fig. 1: Space debris distribution in low earth orbit (Ref. 1)

Different countermeasures can be adopted in dependence of space debris size, currently larger space debris are constantly tracked by ground based surveillance facilities (radar or optical), in order to maintain a catalogue of orbiting debris and eventually to foresee avoidance maneuvers for operative satellite. Nevertheless these monitoring systems cannot identify small debris (1-10 cm) orbiting in the most crowded zone (heights from 700 to 900 km) without a preliminary definition of their orbital parameters. Satellites orbiting in these zones use shields to protect against debris but usually these are effective only for debris smaller than 1 centimeter.

Thus the proposed mission objective is the in-situ surveillance of these zones. The mission is based on a formation of three cooperating satellites, boarding optics and sensors sensible to infrared

or visible radiation, to monitor the LEO space debris environment. The expected results are not only debris detection, but also preliminary orbit determination, thus simplifying follow-up ground based observations.

One larger satellite (a cube with 80 cm side), boarding a larger telescope is adopted for preliminary debris identification and orbit determination, two smaller satellites (two cubes, with 40 cm side), with fast attitude control, are exploited for follow-up debris observation. This mission will permit to improve small space debris orbit knowledge. Through in-orbit collected data the ground based facilities can maintain a catalogue and track the detected debris. In order to maximize the number of observable debris, the formation is designed to fly in circular orbit at 700 km height, the satellites observe in direction of local vertical towards the zenith. As study case an inclination of 65° (launch inclination for DNEPR launcher from baykonour in kazahstan) is analysed in the following.

The simulation that has been carried out, based on statistical knowledge of space debris flux in the heights between 700 and 900 km, showed that more than 200 objects larger than 1 centimeter, cross every day large satellite's telescope field of view.

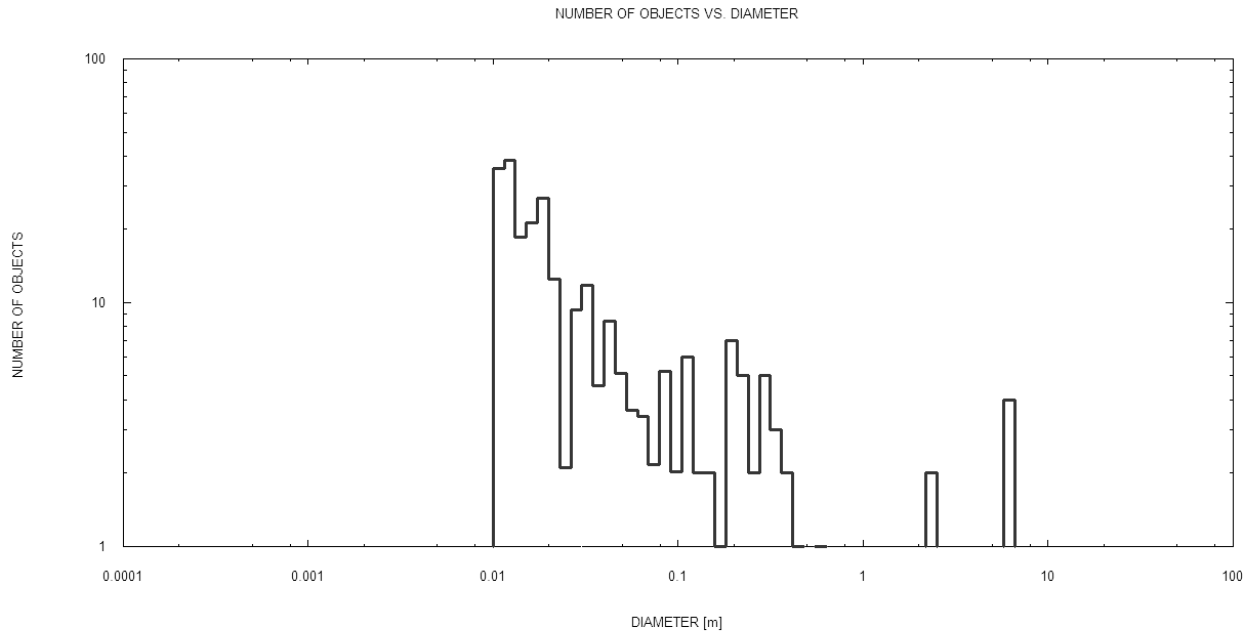

Fig. 2: Detectable space debris diameter distribution

Results of simulations are given in Figure 2 where diameter distribution of detectable objects is reported; it is possible to see that few objects are larger than 10 centimeters and the largest part of them ranges between 1 and 10 centimeters.

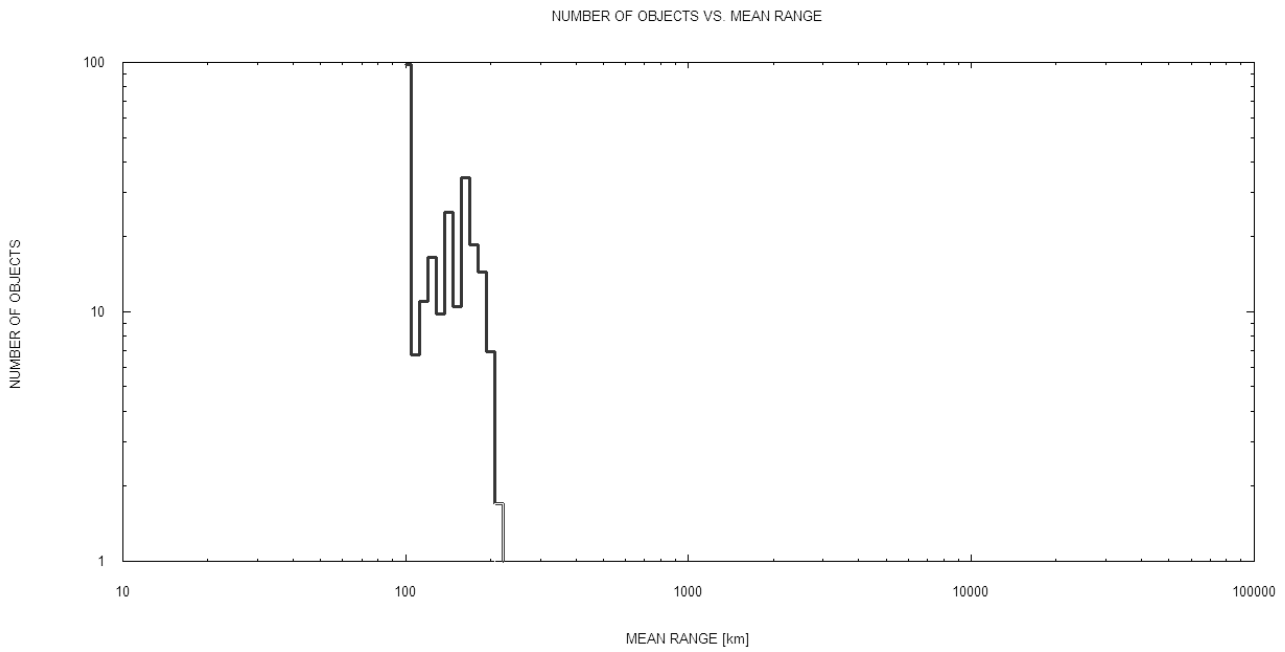

Fig. 3: Detectable space debris mean range distribution

Figure 3 sketches the expected mean range between satellites and observed debris, all of them lies between 100 and 200 km of distance, it has to be noticed that closer debris have not been considered because they are too fast to be tracked by smaller satellites for follow up observations.

The payloads boarded on formation flights satellites are their imaging systems, essentially these systems are a telescope and a CCD (Charge Coupled Device) to take images. The capabilities of the imaging system to catch small debris has been analyzed in function of phase angle (angle between sun-debris-satellite) and range. Payload sizing showed that a 20 centimeter diameter telescope with a CCD with peak quantum efficiency of 60% (in the range of commercial off the shelf CCD) is capable to detect four centimeter size objects crossing at 200 km of distance and a one centimeter object crossing at 100 km of distance. In Figure 4 results of this analysis are sketched, the electrons read-out over noise threshold is given with respect to different phase angles, distances and objects diameter.

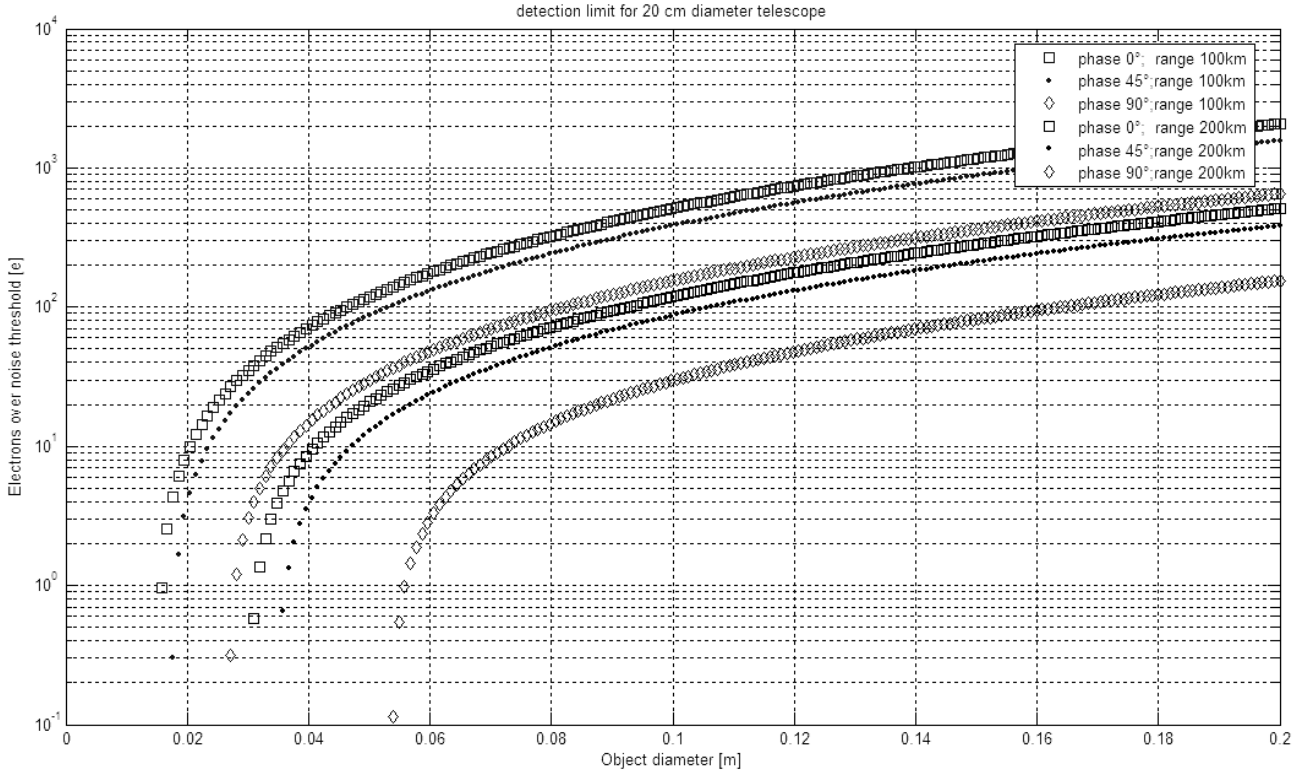

Fig. 4: Optical system sizing for small debris in-orbit detection

Defined this area of interest, a relation between the telescope Field of View and satellite spacing is established. In particular the desired configuration is the one that allows all the three satellites to watch the same area above the central one. This is necessary because in this way the small satellites will start the tracking with a good initial pointing.

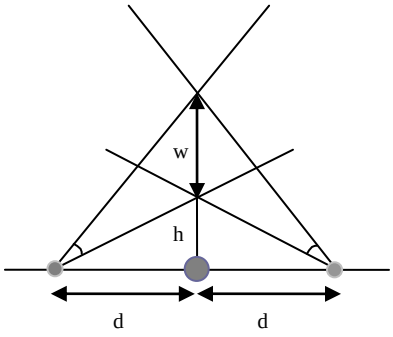

Fig. 5: Sketch of the configuration

If the satellites in the formation are close enough, we can assume that they lie on the same straight line, neglecting in this way the effect of the curvature of the orbit (which results in a very small term). A representation of this configuration is shown in the figure above, where the fields of view of the two smaller satellites have an overlapping observing zone which has a depth w and is

positioned at a distance h above the greater satellite. The relationship between these parameters and the distance d from one satellite to the other is shown in the next equation:

$$FOV = \pi - \arctan\left(-\frac{d}{h}\right) - \arctan\left(\frac{d}{h+w}\right)$$

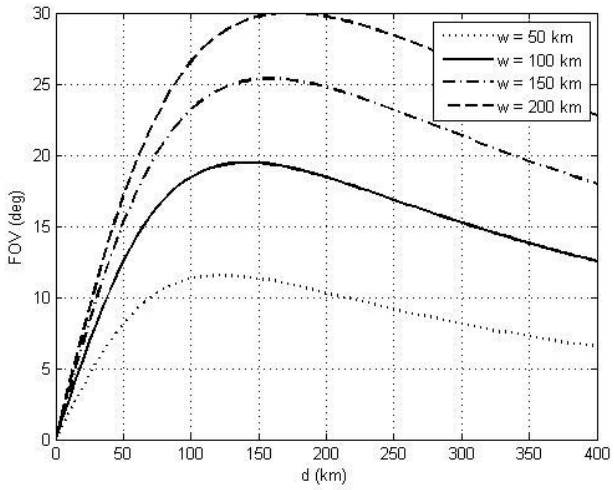

Fig. 6: Different trends of the FOV of the small satellites as a function of distance and depth of the shared field of view

Fig. 6 depicts different trends of the FOV of the small satellites as a function of parameters d and w. With the values selected for the parameters (h = 100 km; w = 100 km; FOV = 12°) a spacing of about 50 km between the satellites is suitable for the proposed mission.

3. Formation maintenance

Maintenance of the formation is a primary task: all along the mission time a maximum tolerance of 10 km in the relative position of the satellites must be assured. Since the two small satellites are identical, the forces they will be subject to will differ only due to their distinct attitude and to possible errors in the initial positioning. In any case the effect of these differences can be controlled with a small effort. Instead, the difference between the forces acting on the big and the small satellites will be much larger and its effect on the formation will be the most relevant. Thus, a good strategy could consist in letting the small satellites free, manoeuvring only the central big satellite. Orbital control on the small satellites will be occasional and is reduced to the minimum: in this way they can be equipped with a very simple orbital control system. In this paper only the manoeuvres for the big satellite will be analyzed. In order to accomplish this goal, it is very useful to consider the relative motion in the orbital rotating reference frame of bigger satellite's theoretical

unperturbed Keplerian orbit. In this case a first-order analysis can be performed, and Euler-Hill equations can be employed.

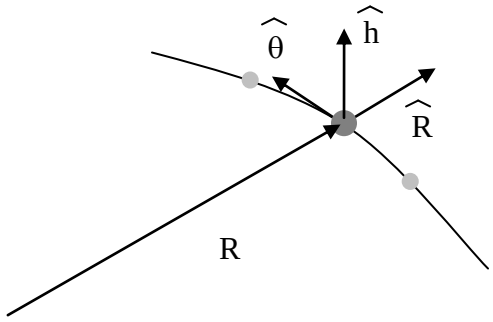

Fig. 7: Rotating Orbital Reference Frame

The equation of motion in a rotating reference frame are:

$$\ddot{\vec{\rho}}+\dot{\vec{\omega}}\times\vec{\rho}+2\vec{\omega}\times\dot{\vec{\rho}}+\vec{\omega}\times\left(\vec{\omega}\times\vec{\rho}\right)=-\frac{\mu}{R^3}\left[\underline{\underline{u}}-3\hat{R}\hat{R}\right]\cdot\vec{\rho}+\vec{f}$$

Where time derivatives are indicated by dots, R is the radius of the Keplerian orbit, while its angular velocity is $\vec{\omega}=\sqrt{\frac{\mu}{R^3}}$, since the reference orbit is circular $\left(\dot{\vec{\omega}}=0\right)$; in the same equation $\vec{\rho}$ indicates the relative position, $\vec{f}$ is the vector of the perturbing accelerations, and the first term on the right-hand side is the Gravity Gradient. Expressing scalar components and switching from time derivatives to angular derivatives (through the expression $\frac{d}{dt}=\vec{\omega}\frac{d}{d\theta}$), the well known Euler-Hill equations can be found:

$$\begin{cases} x''-2y'-3x=\dfrac{1}{\omega^2}f_r \\ y''+2x'=\dfrac{1}{\omega^2}f_\theta \\ z''+z'=\dfrac{1}{\omega^2}f_h \end{cases}$$

In this expression the apex indicates angular derivative, while x, y and z are the scalar components of the vector $\vec{\rho}$ in the $\hat{R}\hat{\theta}\hat{h}$ reference frame ($\vec{\rho}=x\hat{R}+y\hat{\theta}+z\hat{h}$).

The perturbing forces can be divided into two different groups according to their nature: non-gravitational and gravitational perturbations. The first group consists mainly of the aerodynamic drag. Its expression is given by:

$$\vec{f}_a = -\frac{1}{2} C_D \frac{S}{m} \delta v^2 \hat{v}$$

In this case C_D is the drag coefficient of the satellites, whose value can be taken approximately as $C_D \cong 2.2$. S and m are respectively the reference area and the satellite mass. For the big satellite the S/m ratio is equal to 0.007 m2/kg, and for the small ones it is 0.004 m2/kg. Finally δ is the atmospheric density (2.36e-14 kg/m3 at 700 km [6], while v is the satellites' velocity with respect to the inertial reference frame.

The most relevant gravitational perturbation is Earth's oblateness (J2). The related potential is usually expressed by the following expression:

$$U_2 = J_2 \frac{\mu R_\oplus^2}{2} \frac{1}{r^3} \left[1 - 3(\hat{r} \cdot \hat{c}_3)^2\right]$$

Where $J_2 = 1.082e^{-3}$, $R_\oplus$ is Earth's radius and $\hat{c}_3$ is the direction of Earth's spin axis. Then the corresponding expression for the force is:

$$\vec{f}_2 = \nabla(U_2) = -\frac{3}{2} J_2 \mu \frac{R_\oplus^2}{r^4} \left\{ \left[1 - 5(\hat{r} \cdot \hat{c}_3)^2\right] \hat{r} + 2(\hat{r} \cdot \hat{c}_3) \hat{c}_3 \right\}$$

Since a first order analysis is being performed, the perturbations can be evaluated on the reference circular orbit. This means that throughout the study, whatever is the position of the satellites at the current instant of time, the model will consider the forces that would affect the satellites if they lied in the corresponding Keplerian orbit. This hypothesis is supported by the following considerations: for what concerns the aerodynamic drag, the very low order of magnitude of the force assures relatively small deviation from the nominal orbit, while the conservative nature of gravitational perturbations guarantees that they do not affect the energy of the orbit, and consequently do not modify the semi-major-axis.

In this hypothesis, the effects taken into account can be expressed as a function only of the parameters of the associated Keplerian orbit, whose radius and velocity are respectively $\vec{R}$ and $\vec{V}$:

$$\vec{f}_a = -\frac{1}{2} C_D \frac{S}{m} \delta V^2 \hat{V}$$

$$\vec{f}_2 = -\frac{3}{2} J_2 \mu \frac{R_\oplus^2}{R^4} \left\{ \left[1 - 5\left(\hat{R} \cdot \hat{c}_3\right)^2 \right] \hat{R} + 2\left(\hat{R} \cdot \hat{c}_3\right) \hat{c}_3 \right\}$$

Remembering that in a circular Keplerian orbit velocity is given by $\vec{V} = \sqrt{\frac{\mu}{R}}\,\hat{\theta}$, the drag acceleration becomes:

$$\vec{f}_a = -\frac{1}{2} \mu C_D \frac{S}{m} \delta \frac{1}{R} \hat{\theta}$$

This means that in the $\hat{R}\hat{\theta}\hat{h}$ reference frame, the acceleration due to the aerodynamic force can be written as follows:

$$\vec{f}_a = \begin{Bmatrix} f_{ar} \\ f_{a\theta} \\ f_{ah} \end{Bmatrix} = -\frac{1}{2} \mu C_D \frac{S}{m} \delta \frac{1}{R} \begin{Bmatrix} 0 \\ 1 \\ 0 \end{Bmatrix}$$

For what concerns the perturbation caused by Earth's oblateness, it is helpful to introduce the orbital parameters *i* and θ, where *i* is the inclination of the Keplerian orbit and θ is the anomaly of the nominal position of the satellite measured starting from the ascending node. In this way, the direction $\hat{c}_3$ can be written as $\hat{c}_3 = (\sin i \sin\theta)\hat{R} + (\sin i \cos\theta)\hat{\theta} + \cos i\,\hat{h}$, and the product $\left(\hat{R} \cdot \hat{c}_3\right)$ becomes $\left(\hat{R} \cdot \hat{c}_3\right) = \sin i \sin\theta$. By substituting this relations, the following expression for $\vec{f}_2$ is found:

$$\vec{f}_2 = -\frac{3}{2} J_2 \mu \frac{R_\oplus^2}{R^4} \left\{ \left(1 - 3\sin^2 i \, \sin^2\theta\right) \hat{R} + \sin^2 i \, \sin(2\theta)\hat{\theta} + \sin(2i)\sin\theta\,\hat{h} \right\}$$

And, in components:

$$\vec{f}_2 = \begin{Bmatrix} f_{2r} \\ f_{2\theta} \\ f_{2h} \end{Bmatrix} = -\frac{3}{2} J_2 \mu \frac{R_\oplus^2}{R^4} \begin{Bmatrix} 1-3\sin^2 i \sin^2\theta \\ \sin^2 i \sin(2\theta) \\ \sin(2i)\sin\theta \end{Bmatrix}$$

With these formulations for $\vec{f}_a$ and $\vec{f}_2$, the Euler - Hill equations system can now be written as:

$$\begin{cases} x'' - 2y' - 3x = \dfrac{1}{\omega^2}\left(f_{ar} + f_{2r}\right) = -\dfrac{3}{2} J_2 \mu \dfrac{R_\oplus^2}{R^4}\left(1-3\sin^2 i \sin^2\theta\right) \\ y'' + 2x' = \dfrac{1}{\omega^2}\left(f_{a\theta} + f_{2\theta}\right) = -\dfrac{1}{2}\mu C_D \dfrac{S}{m}\delta\dfrac{1}{R} - \dfrac{3}{2} J_2 \mu \dfrac{R_\oplus^2}{R^4} \sin^2 i \sin(2\theta) \\ z'' + z' = \dfrac{1}{\omega^2}\left(f_{ah} + f_{2h}\right) = -\dfrac{3}{2} J_2 \mu \dfrac{R_\oplus^2}{R^4}\sin(2i)\sin\theta \end{cases}$$

Or in matrix form:

$$\begin{Bmatrix} x \\ x' \\ y \\ y' \\ z \\ z' \end{Bmatrix}' = \begin{bmatrix} 0 & 1 & 0 & 0 & 0 & 0 \\ 3 & 0 & 0 & 2 & 0 & 0 \\ 0 & 0 & 0 & 1 & 0 & 0 \\ 0 & -2 & 0 & 0 & 0 & 0 \\ 0 & 0 & 0 & 0 & 0 & 1 \\ 0 & 0 & 0 & 0 & -1 & 0 \end{bmatrix} \begin{Bmatrix} x \\ x' \\ y \\ y' \\ z \\ z' \end{Bmatrix} + \frac{1}{\omega^2} \begin{Bmatrix} 0 \\ -\dfrac{3}{2} J_2 \mu \dfrac{R_\oplus^2}{R^4}\left(1-3\sin^2 i \sin^2\theta\right) \\ 0 \\ -\dfrac{1}{2}\mu C_D \dfrac{S}{m}\delta\dfrac{1}{R} - \dfrac{3}{2} J_2 \mu \dfrac{R_\oplus^2}{R^4} \sin^2 i \sin(2\theta) \\ 0 \\ -\dfrac{3}{2} J_2 \mu \dfrac{R_\oplus^2}{R^4}\sin(2i)\sin\theta \end{Bmatrix}$$

Introducing:

$$Y = \begin{Bmatrix} x \\ x' \\ y \\ y' \\ z \\ z' \end{Bmatrix},\ A = \begin{bmatrix} 0 & 1 & 0 & 0 & 0 & 0 \\ 3 & 0 & 0 & 2 & 0 & 0 \\ 0 & 0 & 0 & 1 & 0 & 0 \\ 0 & -2 & 0 & 0 & 0 & 0 \\ 0 & 0 & 0 & 0 & 0 & 1 \\ 0 & 0 & 0 & 0 & -1 & 0 \end{bmatrix} \text{ and } B = \frac{1}{\omega^2} \begin{Bmatrix} 0 \\ -\dfrac{3}{2} J_2 \mu \dfrac{R_\oplus^2}{R^4}\left(1-3\sin^2 i \sin^2\theta\right) \\ 0 \\ -\dfrac{1}{2}\mu C_D \dfrac{S}{m}\delta\dfrac{1}{R} - \dfrac{3}{2} J_2 \mu \dfrac{R_\oplus^2}{R^4} \sin^2 i \sin(2\theta) \\ 0 \\ -\dfrac{3}{2} J_2 \mu \dfrac{R_\oplus^2}{R^4}\sin(2i)\sin\theta \end{Bmatrix}$$

the previous equation becomes:

$$Y' = AY + B$$

As an outcome of performing a first order analysis, this set of equations results to be linear, so the solution of the system can be written as follows:

$$Y = W \cdot Y_0 + Y_p$$

The matrix W is the transition matrix of the homogeneous system, Y_0 is the initial state in the relative reference frame and Y_p is a particular solution of the non homogeneous problem.

The matrix W is given by:

$$W = \exp(A) = \begin{bmatrix} (4-3\cos\theta) & \sin\theta & 0 & 2-2\cos\theta & 0 & 0 \\ 3\sin\theta & \cos\theta & 0 & 2\sin\theta & 0 & 0 \\ (6\sin\theta-6\theta) & (2\cos\theta-2) & 1 & (-3\theta+4\sin\theta) & 0 & 0 \\ (6\cos\theta-6) & -2\sin\theta & 0 & (-3+4\cos\theta) & 0 & 0 \\ 0 & 0 & 0 & 0 & \cos\theta & \sin\theta \\ 0 & 0 & 0 & 0 & -\sin\theta & \cos\theta \end{bmatrix}$$

The particular solution can be found instead through the following formula:

$$Y_p(\theta) = W(\theta)\int_{\theta_0}^{\theta} W^{-1}(\tau)B(\tau)d\tau$$

Since this is a linear system, it is possible to analyze separately and independently the effects of $\vec{f}_a$ and $\vec{f}_2$, and then superimpose them back again. Then Y_p can be split in $Y_p = Y_{ap} + Y_{2p}$.

Y_{ap} is the particular solution of the problem which considers only $\vec{f}_a$:

$$Y' = AY + B_a \qquad \text{where} \qquad B_a = \frac{1}{\omega^2}\begin{Bmatrix} 0 \\ 0 \\ 0 \\ -\frac{1}{2}\mu C_D \frac{S}{m}\delta\frac{1}{R} \\ 0 \\ 0 \end{Bmatrix}$$

Using the expression given before and assuming $\theta_0 = 0$, it is easy to find Y_{ap} through simple integration:

$$Y_{ap} = W(\theta)\int_0^{\theta} W^{-1}(\tau)B_a(\tau)d\tau = -\frac{1}{2}\mu C_D \frac{S}{m}\delta\frac{1}{\omega^2 R}\begin{Bmatrix} 2\theta - \sin\theta \\ 2 - 2\cos\theta \\ -\frac{3}{2}\theta^2 - 4\cos\theta + 4 \\ -3\theta + 4\sin\theta \\ 0 \\ 0 \end{Bmatrix}$$

The solution diverges in time due to terms linearly depending on θ and θ^2; however, since the coefficient $\frac{1}{2}\mu C_D \frac{S}{m}\delta\frac{1}{\omega^2 R}$ is very small (of the order of 1e-2 m), all the hypothesis made are still satisfied in the short period.

Otherwise, Y_{2p} is the particular solution of the problem which considers only $\vec{f}_2$:

$$Y' = AY + B_2 \qquad \text{where } B_2 = \frac{1}{\omega^2}\begin{Bmatrix} 0 \\ -\frac{3}{2}J_2\mu\frac{R_\oplus^2}{R^4}\left(1 - 3\sin^2 i\,\sin^2\theta\right) \\ 0 \\ -\frac{3}{2}J_2\mu\frac{R_\oplus^2}{R^4}\sin^2 i\,\sin(2\theta) \\ 0 \\ -\frac{3}{2}J_2\mu\frac{R_\oplus^2}{R^4}\sin(2i)\sin\theta \end{Bmatrix}$$

Assuming once again $\theta_0 = 0$, Y_{2p} can be calculated as done before for Y_{ap}:

$$Y_{2p} = W(\theta)\int_0^{\theta} W^{-1}(\tau)B_2(\tau)d\tau$$

$$= -\frac{3}{2}J_2\mu\frac{R_\oplus^2}{R^4}\frac{1}{\omega^2}\begin{Bmatrix} -\frac{1}{3}\cos^2\theta + \frac{2}{3} - \frac{1}{3}\cos\theta + \frac{1}{3}\cos\theta + \frac{1}{3}\cos^2 i + \frac{1}{3}\cos^2 i\cos^2\theta - \frac{2}{3}\cos\theta\cos^2 i \\ \frac{2}{3}\sin\theta\cos^2 i + \frac{1}{3}\sin\theta + \frac{2}{3}\sin\theta\cos\theta - \frac{2}{3}\cos^2 i\cos\theta\sin\theta \\ -\frac{1}{2}\theta - \frac{3}{2}\theta\cos^2 i + \frac{4}{3}\sin\theta\cos^2 i + \frac{2}{3}\sin\theta - \frac{1}{6}\sin\theta\cos\theta + \frac{1}{6}\cos^2 i\sin\theta\cos\theta \\ -\frac{1}{3}\cos^2\theta - \frac{1}{3} + \frac{2}{3}\cos\theta - \frac{5}{3}\cos^2 i + \frac{1}{3}\cos^2 i\cos^2\theta + \frac{4}{3}\cos\theta\cos^2\theta \\ \sin\theta\sin i\cos i - \theta\cos\theta\sin i\cos i \\ \theta\sin\theta\sin i\cos i \end{Bmatrix}$$

It is interesting to point out that this solution does not present any divergent term in the direction $\hat{R}$: this means that averaging over the orbital period the variation of the radius should be zero. This result is very important because in this case the constant coefficient $\frac{3}{2} J_2 \mu \frac{R_\oplus^2}{R^4} \frac{1}{\omega^2}$ has an order of magnitude of $1e7$ m and any divergent term in such direction would lead to a too large error related to the evaluation of perturbing forces on the Keplerian orbit. Otherwise, there is no constraint over the motion in the direction $\hat{\theta}$. This is a result of the absence of the term y in the Euler – Hill equations: for this reason during the linearization operation there is non no need to make any restriction on the position in that direction.

As a consequence of what has been shown, the solution of the relative motion is:

$$Y = W \cdot Y_0 + Y_{ap} + Y_{2p}$$

The expression presented can now be used to predict the relative motion between one of the small satellites and the bigger one: the other small satellite, which is identical to the first one, will have an identical trajectory.

Then calling Y_1 the state vector of the big satellite in the relative reference frame centred in the corresponding point of the unperturbed Keplerian orbit, and identifying Y_2 as the state vector of the small satellite in the same reference frame (still related to the big satellite's theoretical position), the relative motion *X* between the two of them can be easily found exploiting the solution above proposed:

$$X = Y_2 - Y_1 = W \cdot (Y_{02} - Y_{01}) + (Y_{ap_2} - Y_{ap_1}) + (Y_{2p_2} - Y_{2p_1})$$

Since in this model the acceleration due to Earth's flatness depends only on the position along the referential Keplerian orbit, it will affect both the satellites in same way; in other words:

$$Y_{2p_2} = Y_{2p_1}$$

Then aerodynamic drag is the only perturbing force that has influence on the relative motion between the satellites; it is evident indeed that drag causes a larger acceleration over the bigger satellite, because of its larger S/m ratio ($S/m \approx 0.0071$ m^2/kg for the big satellite and $S/m \approx 0.0040$ m^2/kg for the small ones).

The previous expression can be then rewritten as:

$$X = Y_2 - Y_1 = W \cdot (Y_{02} - Y_{01}) + (Y_{ap_2} - Y_{ap_1}) = W \cdot (Y_{02} - Y_{01}) - \frac{1}{2} \mu C_D \delta \frac{1}{\omega^2 R} \left(\frac{S_2}{m_2} - \frac{S_1}{m_1} \right) \begin{Bmatrix} 2\theta - \sin\theta \\ 2 - 2\cos\theta \\ -\frac{3}{2}\theta^2 - 4\cos\theta + 4 \\ -3\theta + 4\sin\theta \\ 0 \\ 0 \end{Bmatrix}$$

The initial conditions related to the described satellite formation are:

$$Y_{01} = \begin{Bmatrix} 0 \\ 0 \\ 0 \\ 0 \\ 0 \\ 0 \end{Bmatrix} \text{ [m]} \qquad \text{and} \qquad Y_{02} = \begin{Bmatrix} 0 \\ 0 \\ 50e3 \\ 0 \\ 0 \\ 0 \end{Bmatrix} \text{ [m]}$$

Since the acceleration due to aerodynamic drag has components only on the orbital plane, it can be demonstrated that the relative motion out of the orbital plane is not coupled with in-plane motion.

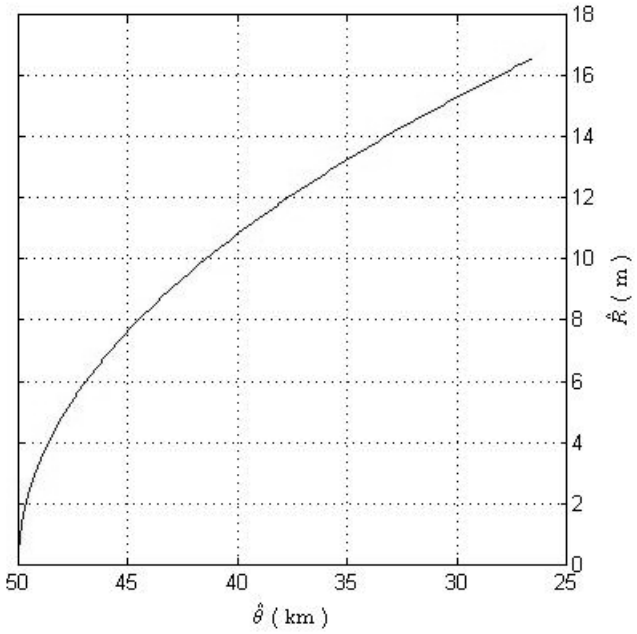

Fig. 8: Relative Motion between the satellites in the $\hat{R}\hat{\theta}$ plane

Fig. 8 shows the relative motion between the two satellites in the $\hat{R}\hat{\theta}$ plane during 150 orbital revolutions. In the graph the two axis are in different scales: the displacement along $\hat{\theta}$ direction is much lager than the displacement along $\hat{R}$. Then, in the scheduling of manoeuvres for the formation maintenance, motion along $\hat{\theta}$ direction will be critical: in fact, the relative positioning constraint of 10 km will be first violated in this direction.

For this reason, Fig. 9 shows the distance between the satellites in that direction as a function of the elapsed orbital revolutions:

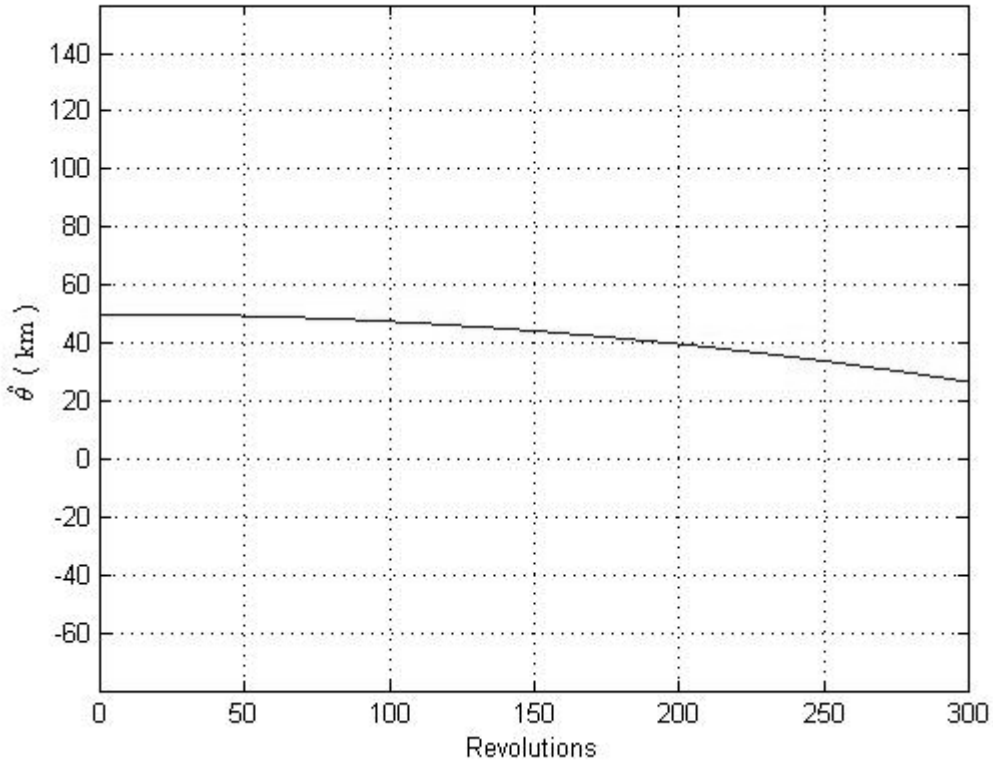

Fig. 9: Distance between the satellites along $\hat{\theta}$ direction as a function of the elapsed orbital revolutions

It has been calculated that after 197 complete revolutions the distance between the satellites along $\hat{\theta}$ direction reduces to less than 40 km, then violating the constraint of 10 km of accuracy in the maintenance of the formation. Given that the period of a circular orbit at an altitude of 700 km is almost 1.65 hours, it will be necessary to operate manoeuvres each 13 and a half days.

It is interesting to analyze how much these manoeuvres cost in the terms of deltavee and propellant; for this reason, the following section will briefly show simple considerations about possible manoeuvres to be operated.

As explained before in the text, formation maintenance has to be performed primarily only the big satellite: as a consequence of this, rather than try to compensate the effects of the drag perturbation on the big satellite, reboosting it on the former nominal orbit, control strategy could plan to reboost the big satellite to the small satellites actual orbit, which will be lower than the previous nominal one. Moreover, since it has been demonstrated that the positioning constraints are violated when the big satellite reaches a distance of only 40 km from the small satellite that precedes it in the formation (on a few meters lower orbit), a good planning could consist in repositioning it 40 km apart from the follower satellite (on a little higher orbit), rather than placing it at the same distance from both the small satellites.

Doing this way, there is no relevant advantage in terms of total ΔV for the mission, but this solution reduces the occurrences of the manoeuvres to be done from twice to once a month.

The correct positioning of the large satellite can be achieved through Hohmann transfers between the starting orbit and a circular parking orbit, and from this to the target orbit, as shown in Fig. 10.

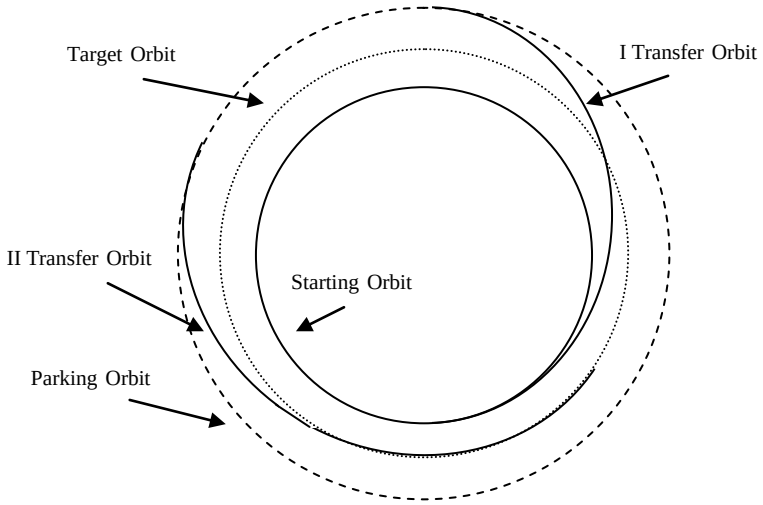

Fig. 10: Manoeuvre Orbital Scheme

While being on the parking orbit, since it is higher than the target orbit, the big satellite will have a smaller angular velocity: in this way the time the second transfer begins can be planned in order to reach the target orbit with the right phase angle.

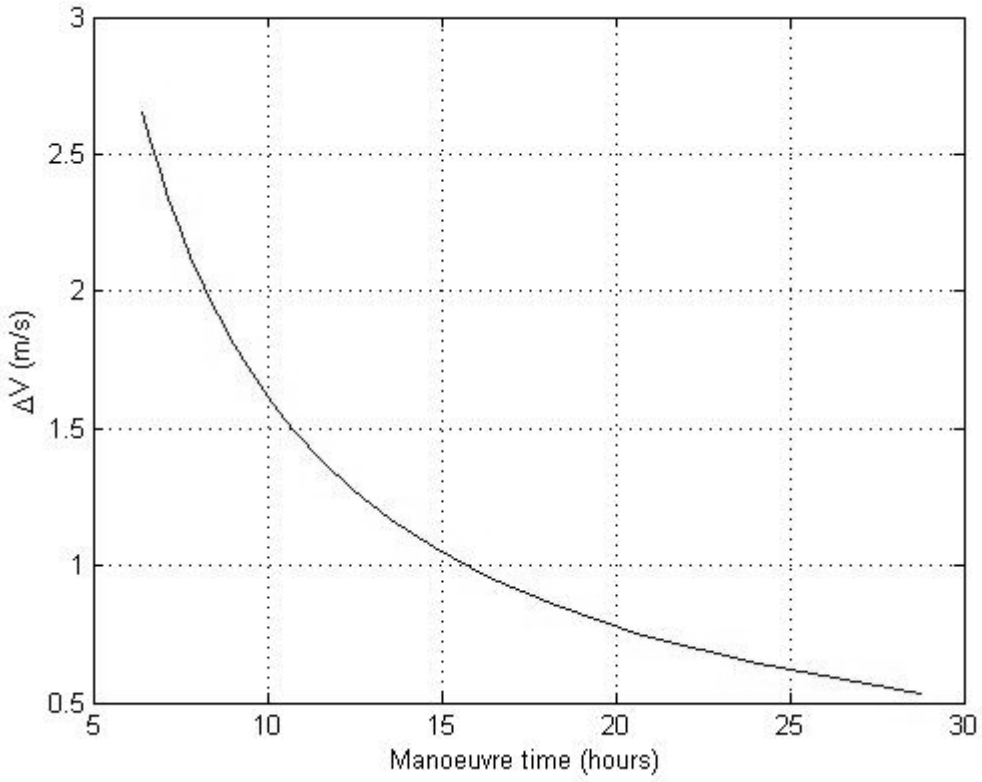

Fig. 11: total ΔV as a function of the time necessary for the manoeuvre

Obviously in this case the apogee of the first elliptical orbit, total ΔV and the time elapsed for the manoeuvres are strictly related: as shown in Fig. 11, the higher the apogee, the faster and the more expensive in terms of ΔV is the formation maintenance. In fact raising the semi-major axis of the transfer orbit, increases the radius and reduces the angular velocity of the related parking orbit: in this way the time the satellite has to wait in this orbit to reach the correct phase angle will be shorter. If a reasonable time of 15 hours is considered, a 1.05 m/s ΔV is found, which corresponds to a 12.6 m/s ΔV per year. Assuming that the satellite is equipped with 10 kg propellant and a 150 s specific impulse chemical thruster, the total available ΔV will be a little more than 84 m/s, making thus the mission duration about 6.5 years long.

Another way to perform the maintenance of the formation can be analyzed: using electric propulsion, which allows to consider thrusters that can be operated continuously, drag could be partially compensated, so that the sum of the forces acting on each of the three satellites would be the same. For example this goal can be reached employing a pulsed plasma thruster whose impulse bit can be 450 μN·s: accurate value of the applied force can be obtained through the modulation of the burst pulses' frequency ($F = f \cdot I_{bit}$).

4. Debris Tracking Attitude Control System

The two small satellites will have a control mode to track the debris object detected by the bigger one in order to take a larger number of photos and allow for a better orbit determination.

The control law proposed to this tracking mode is based on quaternion feedback and is demonstrated to be stable for large (non-linear) rotations [7].

$$\vec{T} = -T_c\left[K\vec{q} + K_i\vec{\omega}\right]$$

The control laws express the torque that must be obtained with the reaction wheels as a function of the angular velocity (ω) and the vector part of the attitude error quaternion; the Tc K Ki gains are tuned using a complete three axis non linear simulation of real cases tracking performed in a simulink environment.

The Actuators selected are four reaction wheels disposed along four different axis in order to achieve redundancy. The Momentum Dumping for the reaction wheel assembly is obtained by the use of Magnetic Torquers.

The state at the beginning of the tracking mode is determined using Earth and Sun-sensors and a star tracker; during the tracking manoeuvre the attitude and angular velocity are determined using Rate Integration Gyros.

In figure (Fig. 12) is shown a functional diagram of the satellite and also of the simulation model. The given values are the satellite's Moments of inertia and the Initial Conditions of the Attitude of the Satellite and the motion of the Target; superimposed to both this Initial Conditions are the errors due to the star tracker and Sun/Earth Sensor for the attitude at the beginning of the manoeuvre; and the errors due to the orbit determination of the big satellite for the target's initial conditions.

The attitude of the satellite is determined by the torques applied; this torques are the sum of the desired control torques plus the errors given by their realization with the reaction wheel. The Angular motion of the satellite is sensed using Rate Integrating Gyros, which also introduce errors, both in attitude and in angular velocity determination. The required control torques are determined using estimated information both for the value of angular velocity and for Attitude Error.

The Attitude Error is evaluated using the estimations of the current attitude and the requested one; the requested attitude for pointing is evaluated using an estimation of the current actual target's position obtained with a model of the relative motion that takes in input the Bigger satellite's Estimation of the target's Initial Conditions, using a Kalman Filter to improve this

estimation and hone the target position prediction. The Kalman Filter takes as input measurements of the Target position performed by the on board camera when the Target is in the Field of View of the telescope.

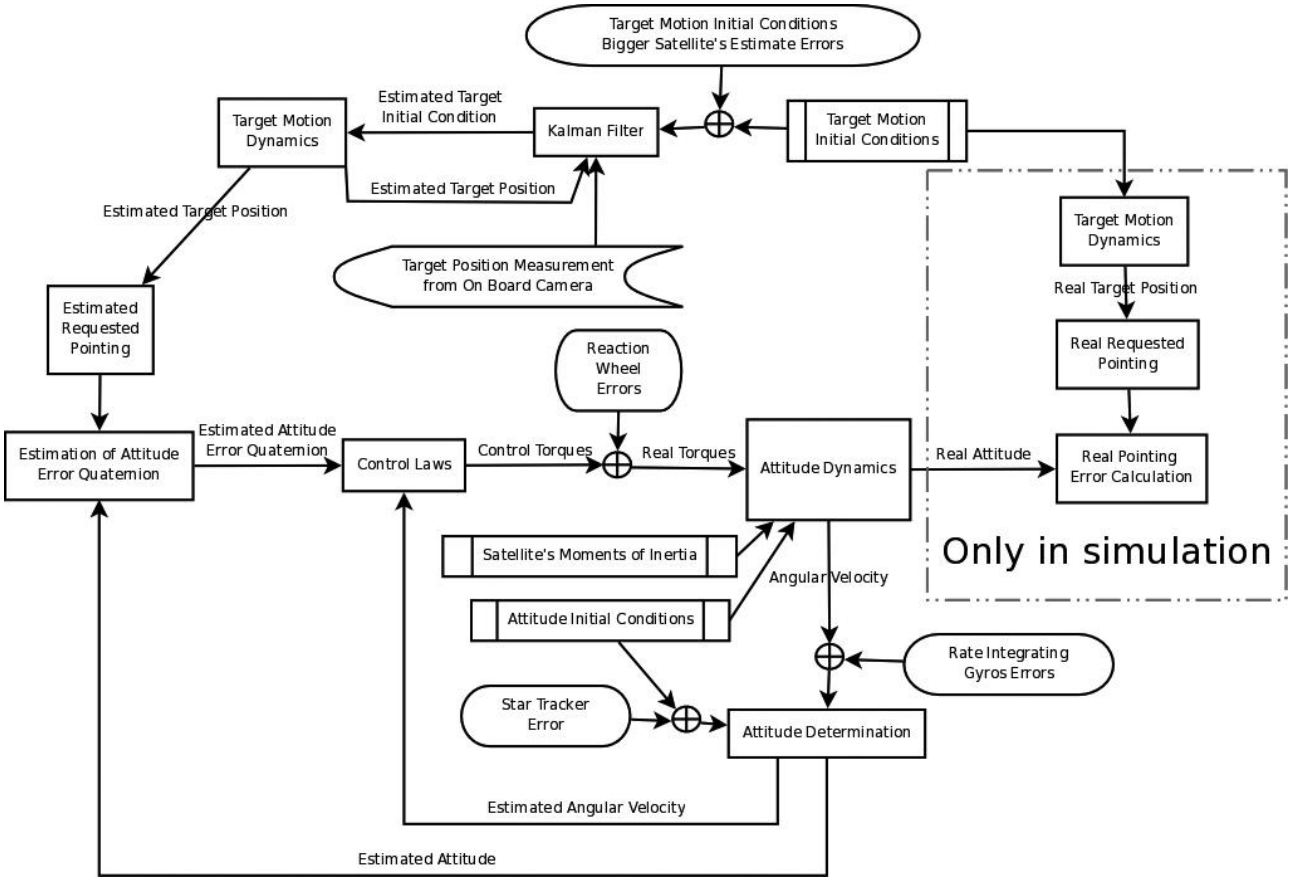

Fig. 12 System Functional Diagram Showing also simulation blocks.

In the Simulation we have access to estimated and measured values but, also, to the "real" initial condition, position, attitude etc. we can the use the model of relative motion to calculate the Target's real position of and the real requested pointing in order to evaluate the real attitude error.

To evaluate the performance of the system a montecarlo method is used performing a large number of simulation introducing the errors like random values with the statistical distribution expected for the real instruments.

This analysis highlighted the key factor of a success tracking, i.e. one in which after less than 10 second the pointing error reach a steady value less than a quarter of the Field of View, is the standard deviation of the Target Initial Condition.

This is clearly explained considering that if the starting Initial Condition Error is too large the target can go out of the field of view of the satellite before the convergence of the kalman filter is reached and then the kalman filter can't be used anymore (because Target Position can't be measured if target is out of Field of View) to hone the estimation of the target Initial Condition; then the pointing error will never be recovered.

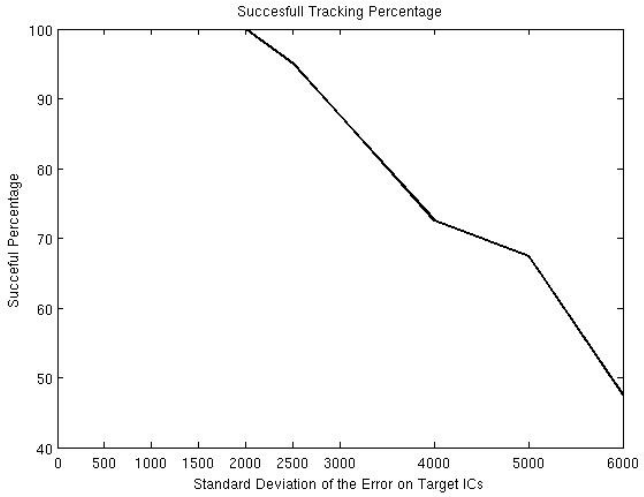

Fig. 13 Successful Tracking Percentage

Figure Fig. 13 shows the successful tracking's percentage as a function of the standard deviation of errors on the determination Target's Initial Conditions; the trend shows a saturation to full success for small standard deviation, when almost all the errors keep the target inside the field of view and can be corrected with the kalman filter, and then the success percentage starts to decrease when the percentage of error that doesn't allow camera measurement begin to raise; the expected standard deviation for the bigger satellite will be in the saturation zone.

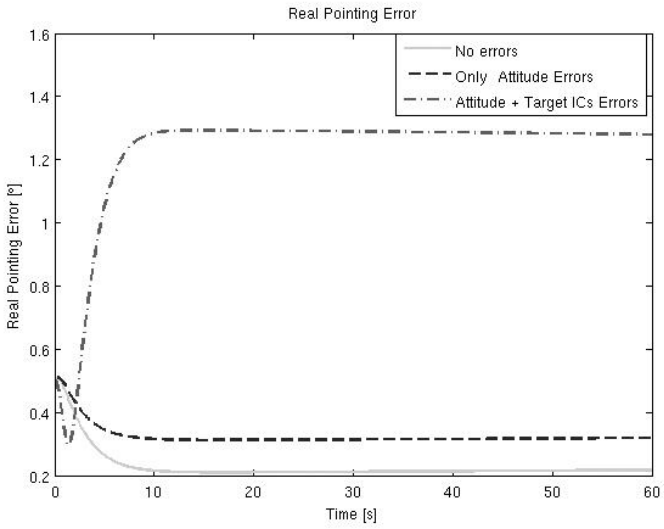

Fig. 14Pointing Error During Manoeuvre

In Figures (Fig. 14 to Fig. 16) are shown the results of a tracking simulation of the same initial condition in three cases, without errors at all, with satellite's attitude errors and, the third, with also the expected error on the target initial conditions; in the graphs are showed the time trend of the real pointing error in figure (Fig. 14), of the torque in figures (Fig. 15) and of the angular momentum accumulated in the wheels in figure (Fig. 16).

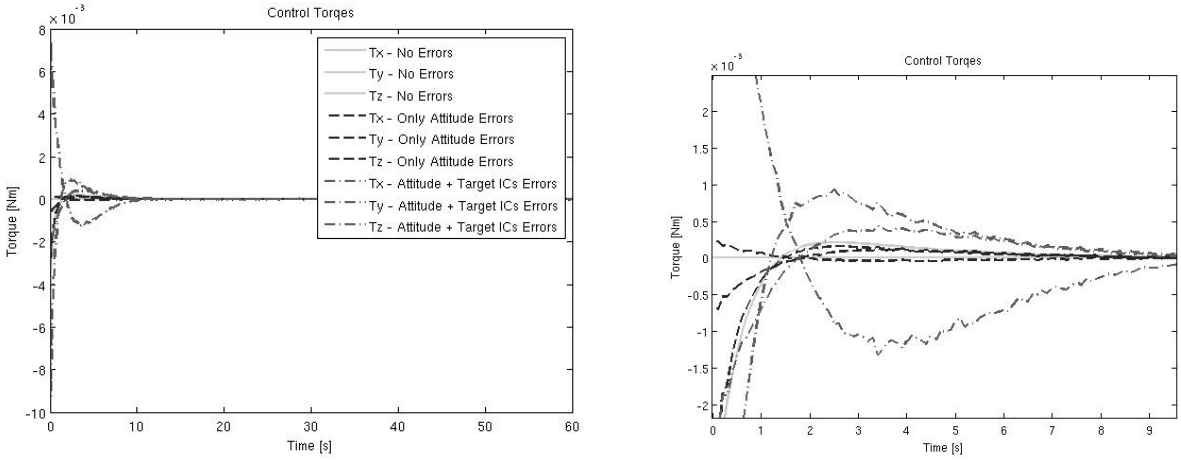

Fig. 15 Control Torques During Tracking Manoeuvre

In the figures is shown how the primary influence is given by the error on the target's initial conditions' estimation. As can be seen it gives a sensible increment on the pointing error, and then also in the required torque; in the torque's graphic the introduction of the attitude error makes the required torque "less smooth" but the values don't have a sensible increase, meanwhile introducing the target's initial conditions errors the values of the required torques have a sensible increase. See the enlargement shown on figure.

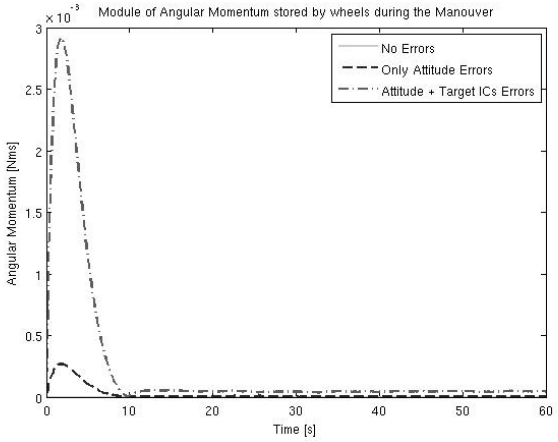

Fig. 16 Wheels' Angular Momentum during Manoeuvre

5. In-orbit automatic image processing

In this mission, frames taken from the in-orbit telescope have to be automatically on-board processed in order to carry out the orbit determination. This is the reason why a software has been developed by G.A.U.S.S. to carry out automatic image processing, in order to detect the debris and identify their position in the field of view of each image.

During the images acquisition, the in-orbit telescope is fixed with respect to the orbital reference frame. With this acquisition mode, the stars result in a trailing trace. The length of the trace is directly proportional to the angular velocity of the space telescope (if the exposure time is

reasonably small, the stars result point shaped). However the objects detected in each image can appear stripe or point shaped, and it depends on relative velocity between the telescope and the target object detected in the frames.

Two different relevant situations have been analyzed when the larger satellite takes images:

1. BEST CASE: the telescope takes frames at the node of its orbit, and the detected objects in the image have the same inclination, right ascension of the ascending node and argument of the perigee orbital parameters.

2. WORST CASE: the satellite and the target object fly with an intersection angle between the orbits of 60°.

In this mission a 1K×1K, 16-bit, camera was considered.with the optical system FOV of 10° and pixel angular dimension of about 35 arcsec.

1- Best case

With this optical system and with the exposure time of 5 seconds, the stars are stripe-shaped and the trace length is about 30 pixel (zoom area in Fig. 17). The orbital angular velocity of the telescope ω_1 at 700 km of height (the velocity v_1 is about 7.4 km/s) is about $\omega_1 = 216$ arcsec/s. For this reason, according to the pixel dimension, it is possible to obtain star stripe length in function of the pixels number.

Objects with a small relative velocity (in the "best case" the telescope and the target object have the same velocity vectors direction and orientation) appear like trailing trace. In this case, the target objects are small stripes or point-shaped (zoom area in Fig. 17). For example, when the telescope and the target object have the same direction and orientation of the velocity vector, and the second one has an altitude of 800 km (with an exposure time of 5s), the apparent displacement of the object detected is about 15 pixels (zoom area in Fig. 17).

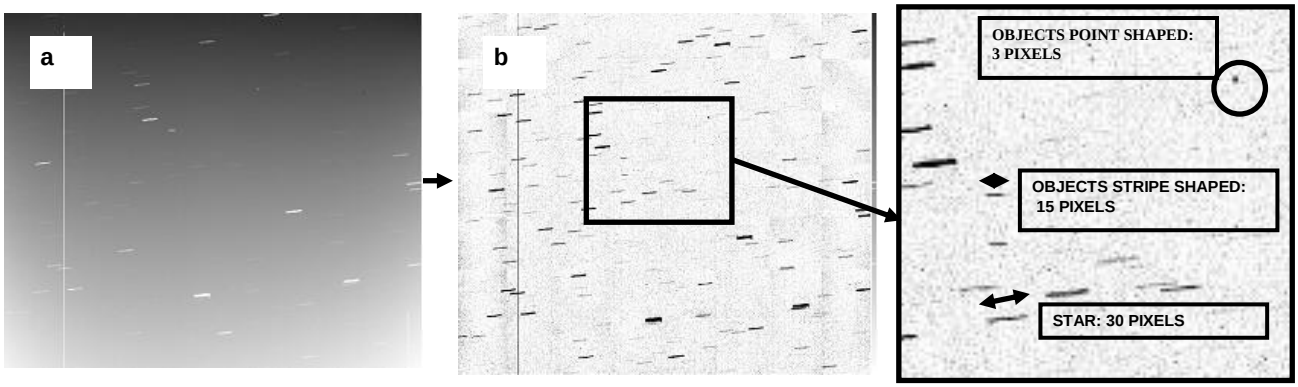

Fig. 17: Simulation of an image taken in the in best case and a zoom area.

Noise reducing-Single frame processing

As shown in Fig. 17-a, the raw images can be affected by a large amount of noise and noise gradient, diverse in different parts of the image. A number of operations could be automatically in-orbit performed on the raw frames in order to obtain a result image (Fig. 17-b) so that the light levels of the lowest signals are similar in the different parts of the image, and the thresholds, to discriminate the signal from the noise, are as uniform as possible. These algorithms have been designed, developed and tested by G.A.U.S.S. in the framework of the realization of the First Italian Observatory fully dedicated to space debris monitoring [9].

Star background removing-Close images mask subtraction

After all of the images of a sequence have been singularly processed, the result is a flat noise level, that is necessary in order to discriminate the target objects from the noise. This second part of the image processing procedures is based on the comparison between the nth image and a close image mask. It can be performed if the images of the sequence are close in time and it is needed to remove the stars background (all the images of the sequences have not the same star field). For example, in Fig. 18 is showed a five image sequence, with an exposure time E.T. = 5s. The time between each image $\Delta T = 30$ seconds. This is the reason why the relative motion of the stars in the successive images is about 180 pixel (trace A in Fig. 18), and about 100 pixel for the stripe shaped object (traces B in Fig. 18).

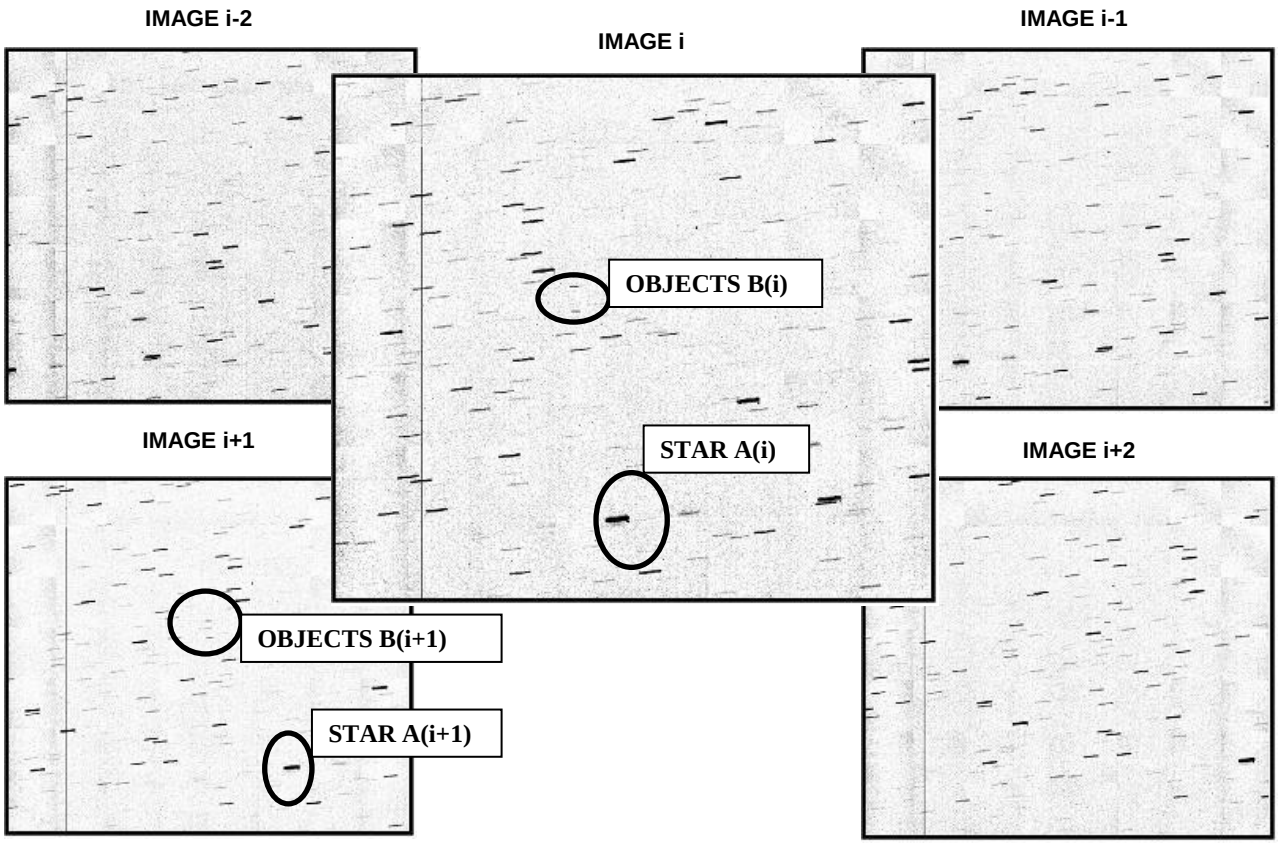

Fig. 18: Images sequence taken in the best case. FOV = 10°. CCD Sensor 1Kx1K. E.T. = 5s. ΔT = 30s.

In order to create the four close image mask, it is important to determinate the displacement of the stars in the FOV of each image. This procedure is organized in three steps:

1. In the first and in the second frames of the sequence it is possible to select 3 apparent star centroids of the same stars.
2. Comparing the coordinates of the centroids in these close images it is possible to estimate the apparent displacement of the stars in the time interval ΔT.
3. Each close image is matched on the image i to be processed.

In Fig. 19 are shown the results of the matching procedure. In this case the displacement between two close images is of 180 pixel in horizontal direction.

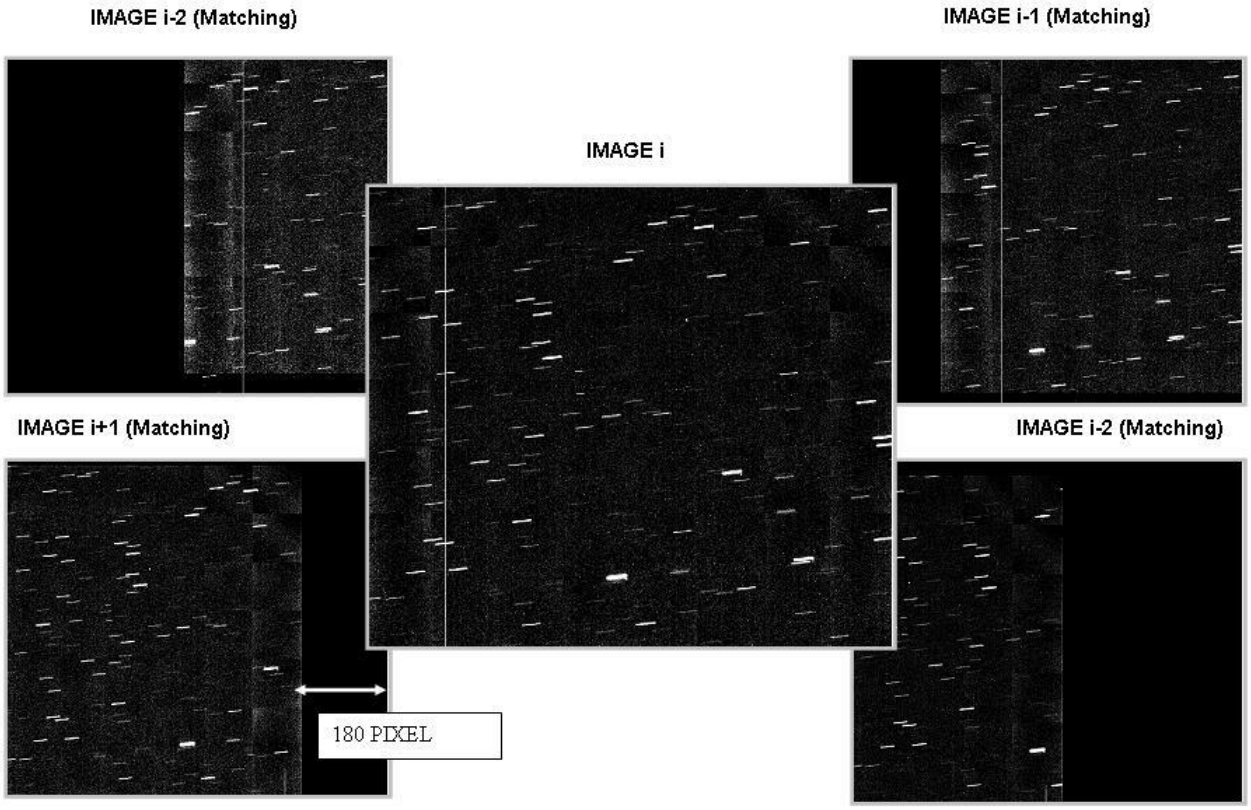

Fig. 19: four close image matching procedure.

Obviously, the mask image is just the sum of the four close images matched (Fig. 20-b). Removing the mask from the original image (Fig. 20-a) it is possible to obtain a result image (Fig. 20-c) in which all the light pixels belonging to the stars are deleted.

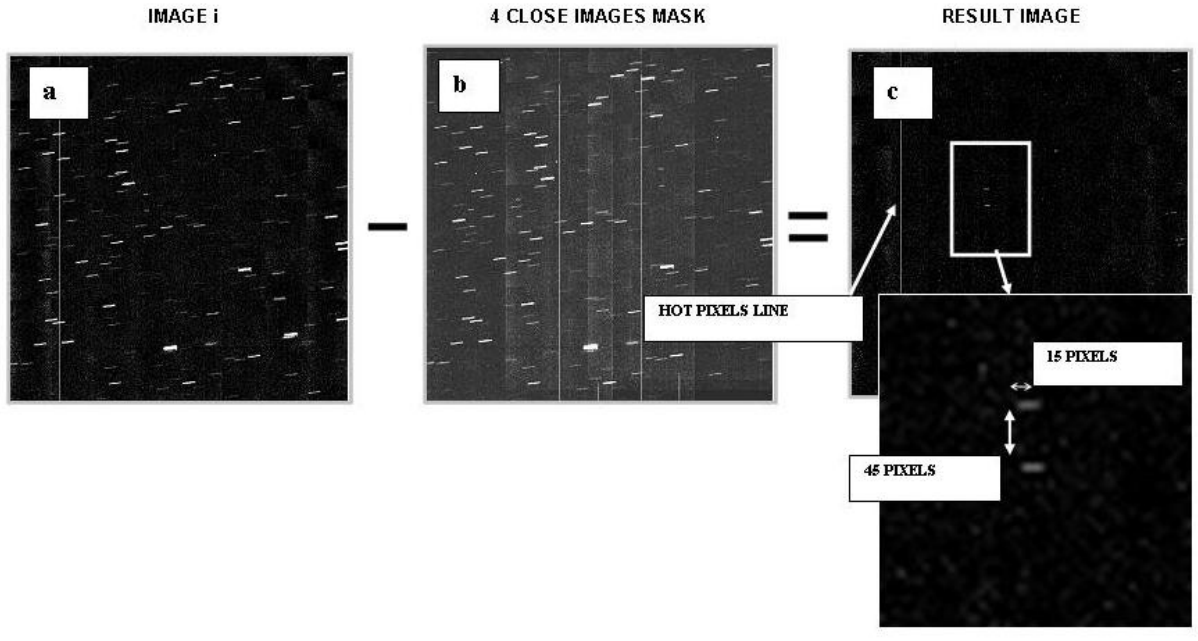

Fig. 20: result of the four close images mask subtraction from the original image.

Object detection procedure

However it can not be excluded that some false signals survive the cancellation procedures (hot pixel line in Fig. 20-c). The software automatically discriminates the target from the false signals carrying on a procedure used and tested by G.A.U.S.S. during the design and realization of a software for the automatic space debris detection and identification in the framework of the realization of the First Italian Space Debris Observatory [8]. The algorithm detects objects storing the distances between light pixels, avoiding morphological analysis in order to reduce calculation time. For this reason it is also a good solution for the in-orbit automatic image processing. The whole procedure is sketched in the drawings in Fig. 21:

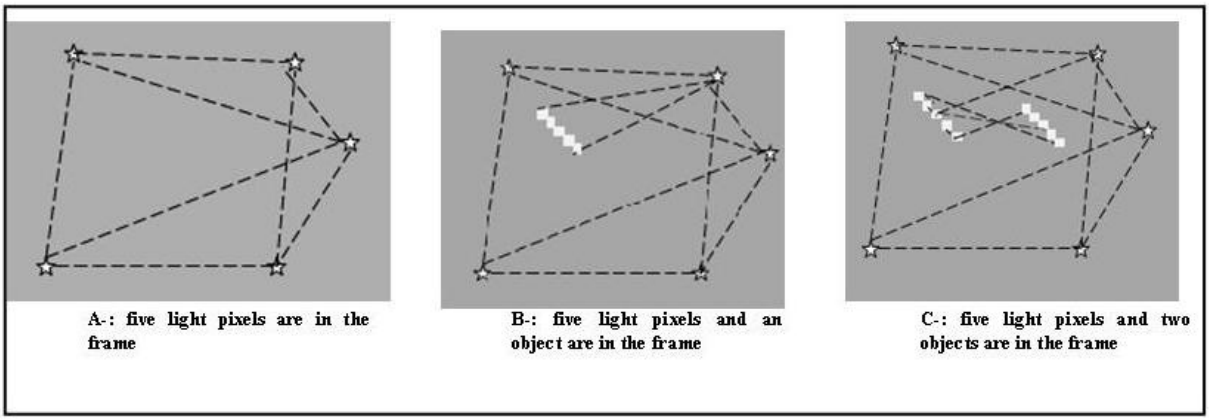

Fig. 21: Object detection procedure.

In Fig. 21-A the reciprocal distances between light pixels are random. In Fig. 21-B there still are 5 light pixels with random distances and a sequence of close pixels belonging to the object. Finally, in Fig. 21-C there are 5 light pixels with random distances and a sequence of close pixels belonging to two objects. Moreover there is a second sequence of light pixels distances due to the two objects mutual distance.

What we have been saying is well clarified by the histograms in Fig. 22: the *x* axis enumerates the distances (in pixels) among all the couples of “luminous” pixels in the frame; the *y* axis reports the number of occurrences for each distance

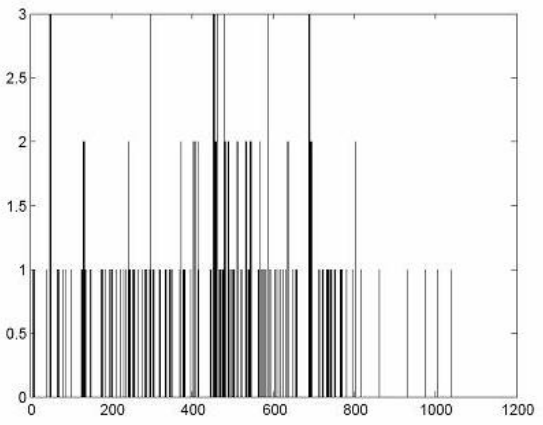

A-: Histogram relevant to a frame without objects. The x axis enumerates the distances (in pixels) among all the couples of "luminous" pixels in the frame; the y axis reports the number of occurrences for each distance.

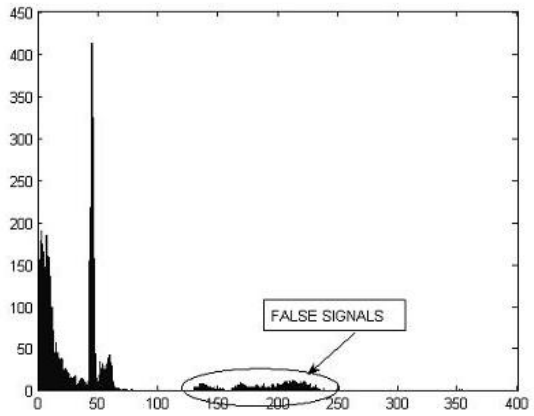

B-: Histogram relevant to the frame shown in -c, featuring two objects. The x axis enumerates the distances (in pixels) among all the couples of "luminous" pixels in the frame; the y axis reports the number of occurrences for each distance.

Fig. 22: Histograms relevant to a frame without objects and to a frame with two objects detected.

Fig. 22-A refers to a frame in which no object is present: the histogram seems to report random distances and the trend is similar to white noise (it refers mainly to the hot pixel line in Fig. 20-c). On the contrary, the histogram in Fig. 22-B shows two peaks at a distance of about 45 pixels which is relevant to the result image in Fig. 20-c. The first peak is due to the great number of occurrences of the small distances between the couples of pixels inside each of the two trails. Accordingly the *x* values are all in the [1, 150] interval. The second peak is due to the mutual distances between the two objects (approximately 45 pixels, see Fig. 20-c). The algorithm also stores the number of peaks in the histogram. In this way, it is possible to detect quickly and fully autonomously the number of objects in a frame, and their coordinates.

2- <u>Worst case</u>

As said before, in the worst case, the space telescope and the target fly with an intersection angle between the two orbits of 60°. For this reason in this case the target relative velocity is bigger than in the best case. In particular a different observation strategy has been studied and, after a trade-off phase, an exposure time of 0.1 seconds has been chosen. This different acquisition mode needs also a small time between two consecutive frames (the time interval ΔT). The whole image processing procedures are sketched in Fig. 23, in which the results have been obtained with a time interval $\Delta T = 0.1$ seconds too.

With the optical system shown above and according to the exposure time E.T. and the time interval ΔT, in this simulation the stars are point shaped and only the high relative velocity objects appears like a trailing trace (Fig. 23-a). In fact, the angular velocity of the in-orbit telescope (which is at an altitude of 700 km) is $\omega_1 = v_1/R_T = 216$ "/s = 6 pixels/s, so that in the whole duration of the exposure time the light from a star is collected by the same pixels region.

This is also the reason why the star field is fixed in the FOV of two consecutive frames. In fact the apparent displacement of the stars in the interval time ΔT = 0.1 is about of 0.6 pixel (star a in Fig. 23-a and Fig. 23-b). This displacement can be easily estimated and removed with the matching procedure showed in the best case image processing software.

On the contrary, the relative velocity between the space telescope and the target could be in the worst case simulation (shown in Fig. 23-a) of about 3.7 km/s. It means that the target apparent displacement in the FOV of the image is about 1400 arcsec (40 pixels in the zoom area in Fig. 23-c).

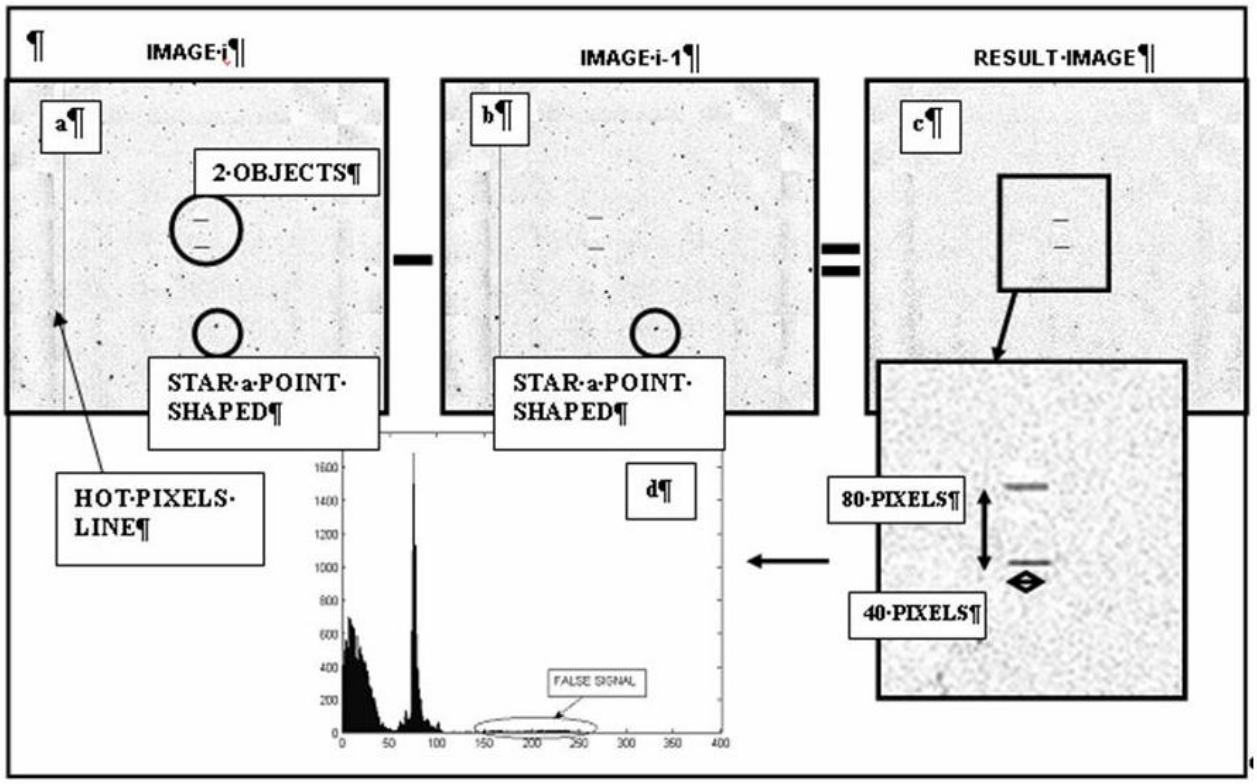

Fig. 23: Results of the automatic image processing and object detection procedures in the worst case.

Noise reducing-Single Frame Processing

The single frame processing procedure is the same employed in the best case simulation, and the two close frames (the image i and image i+1 in Fig. 23-a and Fig. 23-b) shows the results goodness of this algorithm in this different acquisition mode.

Star background removing-Two frame processing

The second part of the automatic image processing software is different in this worst case simulation. It is based on a two close frame (the image i and image i+1 in Fig. 23-a and Fig. 23-b) comparison procedure in which each frame is subtracted the previous one (the star field is fixed in the FOV of two consecutive frames). With this method, the lighting pixels belonging to stars and biases are mostly deleted (Fig. 23-c). It is also a low calculation time procedure and it could be implement on a on-board satellite computer.

Obviously, when one of the two different acquisition strategies is chosen during the mission, the on-board computer has to select the relative automatic image processing procedure.

Object detection procedure

Comparing the results of the image processing procedures in both the best case and the worst case (Fig. 20-c and Fig. 23-c), it is possible to find out that the object detection algorithm showed in the best case, is employable on the worst case too. In fact in the result frame of the automatic image processing procedures the lighting pixels are mainly belonged to the objects detected. However some spurious pixels belonging to false signals survive the cancellation procedure.

So the objects detection procedure employed in the best case can be implemented in this acquisition strategy. The results have been showed in the histogram in Fig. 23-d, relevant to the frame shown in Fig. 23-c. The histogram shows two peaks at a distances of about 80 pixels (distance between the two object in the result image).

Conclusions

The paper shows a possible configuration for a satellite's formation dedicated to in situ space debris detection. A statistical analysis of the number of possible debris detection is presented showing the possible result achievable by the mission. Strategies for formation maintenance and for debris tracking are also presented showing the way and the costs for the mission accomplishment.

Speaking about the realization of a software able to automatically process the in-orbit images sequence, a lot of simulations has been carried out in order to test the algorithms in the two different acquisition modes. The results showed in this paper has been chosen because really representative of the in-orbit operation use. However the objects have been positioned close in the simulation frames in order to show the accuracy of the object detection procedures. In the end, what is also really interesting to remark is that both the noise reducing and objects detection procedures

can be exploited by the software in both the two different acquisition modes. Obviously, the choice of the two different stars background removing procedures is closely related to the kind of the object whose orbit has to be tracked.

Acknowledgements

References

1. M. Porfilio, F. Piergentili, F. Graziani, “First optical space debris detection campaign in Italy”, Advances in Space Research, Vol. 34, n. 5, pp. 921-926, 2004.
2. M. Porfilio, F. Piergentili, F. Graziani, “The 2002 Italian optical observations of the geosynchronous region”, Spaceflight Mechanics 2003, Advances in the Astronautical Sciences, Vol. 114, pp. 1237-1252, Univelt, San Diego, USA, 2003, AAS paper n. AAS 03-186.
3. M. Porfilio, F. Piergentili and F. Graziani, “Two-site orbit determination: The 2003 GEO observation campaign from Collepardo and Mallorca”, Advances in Space Research, Vol. 38, n. 9, pp. 2084-2092, 2006.
4. F. Piergentili, M. Porfilio, F. Graziani, “Optical campaign for low Earth orbit satellites orbit determination”, Proceedings of the Fourth European Conference on Space Debris, ESA SP-587, pp. 689-692, ESA Publications Division, Noordwijk, The Netherlands, 2005.
5. Recent Trends in Satellite Fragmentations, Nasa presentation at opening plenari session, 25th meeting of the IADC, 3-6 July 2007 Toulouse, France.
6. Wiley J. Larson, James R. Wertz, “Space Mission Analysis and Design (Second Edition)”, Kluwer Academic Publishers.
7. Bong Wie, Peter M. Barba (1985), “Quaternion Feedback for Spacecraft Large Angle Manoeuvres” Published on AIAA Journal of Guidance, Control and Dynamics vol.8 n.3-May-june 1985
8. F. Graziani, F. Piergentili, C. Cappelletti, L. Murrali, F. Paolillo, C. Marchiori, M. Porfilio, “The first Italian observatory for space debris observation”, presentato al 58th International Astronautical Congress, Hyderabad 24-28 Settembre 2007, IAF paper IAC-07-A6.I.06.
9. F. Paolillo, M. Porfilio, F. Piergentili, “First Italian space debris observatory: the image processing automation”, 58th International Astronautical Congress, Hyderabad 24-28 September 2007, IAF paper IAC-07-A6.I.05.

Authors

Chantal Cappelletti
School of Aerospace Engineering, University “Sapienza” of Roma, Italy.

Francesco Guarducci
School of Aerospace Engineering, University “Sapienza” of Roma, Italy.

Fabrizio Paolillo
School of Aerospace Engineering, University “Sapienza” of Roma, Italy.

Luigi Ridolfi
School of Aerospace Engineering, University “Sapienza” of Roma, Italy.

Filippo Graziani
Dean of School of Aerospace Engineering, University “Sapienza” of Roma, Italy.

Maria Libera Battagliere
School of Aerospace Engineering, University “Sapienza” of Roma, Italy.

Fabrizio Piergentili
Assistant Professor, DIEM, II Faculty of Engineering, University of Bologna, Forlì, Italy.

Fabio Santoni
Professor of School of Aerospace Engineering, University “Sapienza” of Roma, Italy.